




Cite this: *RSC Adv.*, 2023, 13, 11569

# Synergistic interface between metal Cu nanoparticles and CoO for highly efficient hydrogen production from ammonia borane†

Hongmei Li, Wenxue He, Liuxin Xu, Ya Pan, Ruichao Xu, Zhihu Sun \* and Shiqiang Wei 

The development of efficient non-noble metal catalysts for the dehydrogenation of hydrogen (H<sub>2</sub>) storage materials is highly desirable to enable the global production and storage of H<sub>2</sub> energy. In this study, Cu<sub>x</sub>–(CoO)<sub>1–x</sub>/TiO<sub>2</sub> catalysts with a Cu–CoO interface supported on TiO<sub>2</sub> are shown to exhibit high catalytic efficiency for ammonia borane (NH<sub>3</sub>BH<sub>3</sub>) hydrolysis to generate H<sub>2</sub>. The best catalytic activity was observed for a catalyst with a Cu : Co molar ratio of 1 : 1. The highest dehydrogenation turnover frequency (TOF) of 104.0 mol<sub>H<sub>2</sub></sub> mol<sub>metal</sub><sup>–1</sup> min<sup>–1</sup> was observed in 0.2 M NaOH at room temperature, surpassing most of the TOFs reported for non-noble catalysts for NH<sub>3</sub>BH<sub>3</sub> hydrolysis. Detailed characterisation of the catalysts revealed electronic interactions at the Cu–CoO heterostructured interface of the catalysts. This interface provides bifunctional synergetic sites for H<sub>2</sub> generation, where activation and adsorption of NH<sub>3</sub>BH<sub>3</sub> and H<sub>2</sub>O are accelerated on the surface of Cu and CoO, respectively. This study details an effective method of rationally designing non-noble metal catalysts for H<sub>2</sub> generation via a metal and transition-metal oxide interface.

Received 24th February 2023  
Accepted 4th April 2023

DOI: 10.1039/d3ra01265d

rsc.li/rsc-advances

## Introduction

Hydrogen (H<sub>2</sub>) is a promising alternative to traditional fossil fuels due to its high energy density, sustainability, and pollution-free properties.<sup>1–3</sup> For example, new-energy vehicles use H<sub>2</sub> fuel cells as their power source.<sup>4</sup> However, the wide application of H<sub>2</sub> as a fuel is hindered by difficulties associated with its production, storage, and transportation.<sup>5–8</sup> Exploration of efficient chemical H<sub>2</sub> storage materials for H<sub>2</sub> storage and release has hence attracted extensive attention in recent years. Among these materials, ammonia borane (NH<sub>3</sub>BH<sub>3</sub>) is considered to have many outstanding advantages, such as a high H<sub>2</sub> content (19.6 wt%), high water solubility, non-toxicity, and excellent stability in aqueous solution and air under ambient conditions.<sup>9–11</sup> More importantly, with the right catalyst, NH<sub>3</sub>BH<sub>3</sub> can rapidly and completely release all of its H<sub>2</sub> in aqueous solution at room temperature, as shown in the following reaction equation:



So far, a large number of noble metal catalysts have been demonstrated to exhibit high activity in the hydrolysis of

NH<sub>3</sub>BH<sub>3</sub>.<sup>12–15</sup> Nevertheless, noble metals are costly and scarce, which significantly restricts their wide applications. Thus, cheap and abundant non-noble metal catalysts have attracted increasing attention. However, the design of a non-noble metal catalyst that exhibits high performance and long-term stability still remains a challenge.

Recent studies have shown that some transition metal (TM) catalysts (cobalt (Co), copper (Cu), iron (Fe), nickel (Ni)) exhibit catalytic activity in the hydrolytic dehydrogenation of NH<sub>3</sub>BH<sub>3</sub>.<sup>16–23</sup> Among them, Cu is an abundant element and is one of the TMs with the most potential for NH<sub>3</sub>BH<sub>3</sub> hydrolysis. As the catalytic performance of single metal Cu catalysts is poor,<sup>16,24</sup> bimetallic or polymetallic Cu-based alloys and nanoparticles (NPs) have been extensively explored to improve the activity of Cu-based catalysts.<sup>25–29</sup> The improved performance of polymetallic NPs arises from the synergistic effect of optimised composition and electron transfer between metals. Cu-based alloy catalysts also have limitations towards NH<sub>3</sub>BH<sub>3</sub> hydrolysis as they only activate NH<sub>3</sub>BH<sub>3</sub> molecules,<sup>30</sup> while having only a weak effect on the adsorption and activation of H<sub>2</sub>O molecules, which is the rate-determining step in the hydrolysis reaction. Multiple studies have shown that transition-metal oxides (TMOs) accelerate the activation of water molecules.<sup>31–33</sup> Therefore, a heterogeneous structure incorporating TMOs and metal NPs is an effective strategy for synthesising catalysts for hydrolysis reactions. Xu *et al.* reported that a catalyst with a Cu–Co<sub>3</sub>O<sub>4</sub> interface greatly improves the hydrolysis performance of NH<sub>3</sub>BH<sub>3</sub>; Cu effectively activates

National Synchrotron Radiation Laboratory, University of Science and Technology of China, Hefei 230029, P. R. China. E-mail: zhsun@ustc.edu.cn

† Electronic supplementary information (ESI) available. See DOI: <https://doi.org/10.1039/d3ra01265d>



$\text{NH}_3\text{BH}_3$  molecules and  $\text{Co}_3\text{O}_4$  effectively activates  $\text{H}_2\text{O}$  molecules.<sup>34</sup> Wang and co-authors reported that a  $\text{Cu}/\text{Cu}_{0.76}\text{Co}_{2.24}\text{O}_4$  double active site catalyst modified with oxygen vacancies ( $V_{\text{O}}$ ) significantly increased the  $\text{H}_2$  production rate in the hydrolysis of  $\text{NH}_3\text{BH}_3$ .<sup>31</sup> Zhou *et al.* fabricated  $\text{CuNi}$  bimetallic NPs anchored on  $\text{Co}_3\text{O}_4$  nanosheets, where the synergistic effect between  $\text{Cu}$  and  $\text{Ni}$  species and the strong interactions between  $\text{CuNi}$  and  $\text{Co}_3\text{O}_4$  afforded a maximum turnover frequency (TOF) of  $31.5 \text{ mol}_{\text{H}_2} \text{ mol}_{\text{metal}}^{-1} \text{ min}^{-1}$  in  $0.14 \text{ M NaOH}$  at  $298 \text{ K}$ .<sup>33</sup> However, the addition of ineffective proportions of TMOs with non-ideal compositions leads to catalysts being produced with low intrinsic activity. Therefore, the optimisation of the interfacial effect of metals and TMOs to achieve the best catalytic performance remains a challenging task. Moreover, these metal and oxide NPs tend to aggregate and lead to the deactivation of the reaction being catalysed, which results in greatly reduced stability and repeatability. An effective way to overcome this problem is to find a suitable support. Titanium dioxide ( $\text{TiO}_2$ ) is often used as a carrier for metal nanomaterials due to its excellent properties, such as non-toxicity and stability.<sup>35,36</sup>

In this study, it is reported that high catalytic activity for  $\text{NH}_3\text{BH}_3$  hydrolysis can be achieved over catalysts with a  $\text{Cu-CoO}$  interface.  $\text{CoO}$  was selected to form an heterogeneous interface with metallic  $\text{Cu}$  NPs as  $\text{Co}^{2+}$  ions are in a relatively low oxidation state and therefore have the tendency to donate electrons and form active interfacial sites. A simple impregnation method was used to load  $\text{Cu}^{2+}$  and  $\text{Co}^{2+}$  on a  $\text{TiO}_2$  support, followed by the selective reduction of  $\text{Cu}^{2+}$  using  $\text{NaBH}_4$ , thus leading to the formation of a series of  $\text{Cu}_x-(\text{CoO})_{1-x}/\text{TiO}_2$  samples containing a  $\text{Cu-CoO}$  interface. As expected, all of the catalysts significantly increase the rate of  $\text{NH}_3\text{BH}_3$  dehydrogenation, and a volcano-type curve was obtained. Of the prepared catalysts,  $\text{Cu}_{0.5}-(\text{CoO})_{0.5}/\text{TiO}_2$  exhibits the best catalytic activity, with a TOF of  $104.0 \text{ mol}_{\text{H}_2} \text{ mol}_{\text{metal}}^{-1} \text{ min}^{-1}$  in  $0.2 \text{ M NaOH}$  at room temperature, surpassing the performance of most of the reported  $\text{Cu}$ -based catalysts for  $\text{NH}_3\text{BH}_3$  hydrolysis. This outstanding performance arises from the synergistic interactions between  $\text{Cu}$  and  $\text{CoO}$ , which promote the activation of  $\text{NH}_3\text{BH}_3$  and  $\text{H}_2\text{O}$  molecules, respectively. The hybrid  $\text{Cu}_{0.5}-(\text{CoO})_{0.5}/\text{TiO}_2$  catalyst is simple to synthesise, low cost, high efficiency, and can be widely used in a range of dehydrogenation reactions.

## Experimental

### Catalyst preparation

A series of  $\text{Cu}_x-(\text{CoO})_{1-x}/\text{TiO}_2$  samples were synthesised *via* an incipient wetness impregnation and co-reduction method. The detailed synthesis of  $\text{Cu}_{0.5}-(\text{CoO})_{0.5}/\text{TiO}_2$  is used here as an example. Firstly,  $\text{CuCl}_2 \cdot 2\text{H}_2\text{O}$  (341 mg) and  $\text{CoCl}_2 \cdot 6\text{H}_2\text{O}$  (476 mg) were dissolved in water (14 mL), to which  $\text{TiO}_2$  powder (3.5 g) was added under magnetic stirring. The pH of the solution was kept at 7.0 and the reaction mixture was subjected to ultrasonication for 1 h. The OH groups on the surface of the  $\text{TiO}_2$  support serve as adsorption sites for  $\text{Cu}^{2+}$  and  $\text{Co}^{2+}$  cations. The pH of the solution is higher than the isoelectric point (5.8) of  $\text{TiO}_2$ , which makes the surface of  $\text{TiO}_2$  negatively charged and

favourable for cation adsorption. After drying at  $60^\circ\text{C}$  overnight, the obtained powder was washed with a large amount of ultra-pure water to remove residual chloride ions. The impregnated intermediate was dehydrated at  $60^\circ\text{C}$  to form  $\text{CuO}$  and  $\text{CoO}$  oxides, resulting in the formation of  $(\text{CuO})_{0.5}-(\text{CoO})_{0.5}/\text{TiO}_2$ . Secondly, 350 mg of the above product was dispersed in 50 mL of water, to which 10 mL of an aqueous solution containing 100 mg of  $\text{NaBH}_4$  was added dropwise under vigorous magnetic stirring. When bubbles ceased to be generated in the reaction mixture, the reduction was taken to be complete. Finally, the resulting precipitate was filtered off, washed with water, and dried overnight at  $60^\circ\text{C}$ . By changing the molar ratio of  $\text{Cu}$  to  $\text{Co}$  while keeping the total metal content at 4 mmol,  $\text{CoO}/\text{TiO}_2$ ,  $\text{Cu}_{0.1}-(\text{CoO})_{0.9}/\text{TiO}_2$ ,  $\text{Cu}_{0.3}-(\text{CoO})_{0.7}/\text{TiO}_2$ ,  $\text{Cu}_{0.7}-(\text{CoO})_{0.3}/\text{TiO}_2$ ,  $\text{Cu}_{0.9}-(\text{CoO})_{0.1}/\text{TiO}_2$ , and  $\text{Cu}/\text{TiO}_2$  catalysts were synthesised using the same method.

### Catalyst characterisation

Powder X-ray diffraction (PXRD) analysis was recorded using a Rigaku Miniflex-600 diffractometer operated at a voltage of 40 kV and current of 15 mA using a  $\text{Cu K}\alpha$  radiation source. Inductively coupled plasma atomic emission spectroscopy (ICP-AES, Optima 7300 DV) was used to determine the exact  $\text{Cu}$  and  $\text{Co}$  content in the catalysts. X-ray photoelectron spectroscopy (XPS) was conducted on a Thermo ESCALAB 250 spectrometer using an  $\text{Al K}\alpha$  ( $h\nu = 1486.6 \text{ eV}$ ) excitation source to analyse the elemental valence states of the samples. Energy-dispersive X-ray spectroscopy (EDX) mapping was conducted on a JEOLJEM-ARM200F transmission electron microscope (TEM)/scanning transmission electron microscope (STEM) equipped with a spherical aberration corrector and operated at 300 kV. TEM, high-resolution TEM (HRTEM), and EDX images were obtained on a JEM-2100F instrument operated at an accelerating voltage of 200 kV. Brunauer–Emmett–Teller (BET) specific surface areas of the samples were measured using an automatic volume adsorption device (Micrometrics ASAP 2020).

### X-ray absorption fine structure (XAFS) characterisation

XAFS measurements at the  $\text{Cu K-edge}$  (8979 eV) and  $\text{Co K-edge}$  (7709 eV) were performed at the BL14W1 beamline of the Shanghai Synchrotron Radiation Facility (SSRF) and the 1W1B beamline of the Beijing Synchrotron Radiation Facility (BSRF), China. The storage rings of the SSRF and BSRF were operated at 3.5 and 2.5 GeV in top-up mode, respectively. On both of the beamlines,  $\text{Si}(111)$  double-crystal monochromators were used and detuned by 30% to eliminate the higher-order harmonics. The  $\text{Cu K-edge}$  XAFS spectra were collected in transmission mode, the  $\text{Co K-edge}$  XAFS spectra in fluorescence mode. The ATHENA module implemented in the IFEFFIT software packages was used to process the obtained XAFS data.<sup>37</sup>

### Catalytic activity assessment

The  $\text{H}_2$  generation rate of the hydrolysis of  $\text{NH}_3\text{BH}_3$  was measured *via* the water displacement method. In a typical process, a round-bottom flask (25 mL) containing a magneton was positioned in a water bath to control the temperature at  $298$



K with stirring. The flask was then sequentially filled with 10 mg of the  $\text{Cu}_{0.5}-(\text{CoO})_{0.5}/\text{TiO}_2$  catalyst and 5 mL of an aqueous solution of  $\text{NH}_3\text{BH}_3$  ( $0.065 \text{ mol L}^{-1}$ ). Immediately, the hydrolysis reaction commenced and a large volume of  $\text{H}_2$  was produced and was collected in a water-filled inverted volumetric cylinder. The released  $\text{H}_2$  replaced the water in the cylinder, and the time was recorded after every 1 mL of  $\text{H}_2$  was collected. The activity of the other catalysts was also determined using the above method, while keeping the mass of all of the catalysts at 10 mg. For cycling experiments, the same amount of an aqueous solution of  $\text{NH}_3\text{BH}_3$  was injected into the flask after the previous reaction was completed.

Reactive kinetics measurements were also performed in the same reaction system. To measure the reaction order, the concentration of  $\text{NH}_3\text{BH}_3$  and the mass of the catalyst were varied. Then, based on the rate equation, the rate constant,  $k$ , was obtained:

$$r = -\frac{dC}{dt} = kC^m \quad (2)$$

$$\ln r = n \ln C + \ln k \quad (3)$$

The catalyst concentration,  $C$ , was altered to measure the reaction rate,  $r$ , at different temperatures (298, 303, 308, and 313 K). The intercept obtained by linear fitting gives the reaction rate constant,  $k$ , and thus the apparent activation energy,  $E_a$ , can be obtained according to the Arrhenius equation:

$$\ln k = \ln A - \frac{E_a}{RT} \quad (4)$$

where  $k$  is the reaction rate constant,  $A$  is the pre-exponential factor,  $E_a$  is the activation energy of the reaction,  $R$  is the molar gas constant, and  $T$  is the reaction temperature (K). To evaluate the catalytic activity of hydrolysis, the TOF was calculated using the following equation:

$$\text{TOF} = \frac{n_{\text{H}_2}}{n_{\text{metal}}t} \quad (5)$$

where  $n_{\text{H}_2}$  is the molar amount of generated  $\text{H}_2$ ,  $n_{\text{metal}}$  is the total molar amount of metal species in the catalyst, and  $t$  is the reaction time.

## Results and discussion

### Synthesis and characterisation of the catalysts

Several samples of  $\text{Cu}_x-(\text{CoO})_{1-x}/\text{TiO}_2$ ,  $\text{Cu}/\text{TiO}_2$  and  $\text{CoO}/\text{TiO}_2$  were synthesised on rutile  $\text{TiO}_2$  NPs *via* an incipient wetness impregnation and co-reduction method using  $\text{CuCl}_2$  and  $\text{CoCl}_2$  as raw materials. Reduced Co was coated on Cu particles, but the Co NPs were soon oxidised in the air and co-loaded on the  $\text{TiO}_2$  in the form of a CoO species. The Cu and Co content in these samples was measured by ICP-AES analysis (Table S1†). The total metal content in each catalyst was controlled at around 4 mmol. The PXRD patterns of all of the samples showed no diffraction peaks related to Cu and Co (Fig. S1†), suggesting the small particle size, high dispersion, or amorphous state of the Cu- and Co-related species. Among all the

catalysts,  $\text{Cu}_{0.5}-(\text{CoO})_{0.5}/\text{TiO}_2$  exhibited the highest catalytic activity for  $\text{NH}_3\text{BH}_3$  hydrolysis (*vide infra*), and was thus selected for detailed characterisation.

Fig. 1a shows the TEM images of the  $\text{Cu}_{0.5}-(\text{CoO})_{0.5}/\text{TiO}_2$  catalyst. The surface of the catalyst has a rough appearance, which is very different to the smooth surface of the pristine  $\text{TiO}_2$  support (Fig. S2a†), indicating that small metal NPs are formed on the surface of the  $\text{TiO}_2$  support. Moreover, different from the severe particle agglomeration on the  $\text{TiO}_2$ -free sample  $\text{Cu}_{0.5}-(\text{CoO})_{0.5}$  (Fig. S2b†), the  $\text{Cu}_{0.5}-(\text{CoO})_{0.5}$  NPs on the surface of  $\text{TiO}_2$  in  $\text{Cu}_{0.5}-(\text{CoO})_{0.5}/\text{TiO}_2$  are fine and highly dispersed. The morphology of the  $\text{Cu}_{0.5}-(\text{CoO})_{0.5}/\text{TiO}_2$  catalyst can be more clearly observed from its HRTEM image. As is shown in Fig. 1b, the interplanar spacing of 0.25 nm corresponds to the (101) crystal plane of rutile  $\text{TiO}_2$ , and the other lattice spacing of 0.208 nm can be matched to the (111) crystal plane of face-centred cubic (fcc) Cu NPs. The crystal plane angle between two 111 planes calculated from the atomic spacing obtained by inverse Fourier transform (FT) of the selected region is  $71^\circ$ , which is also characteristic of Cu NPs. The light grey region surrounding the Cu NPs and  $\text{TiO}_2$  lattice is probably related to the CoO species, the lattice stripes of which cannot be observed because of its amorphous state. The corresponding elemental mapping of  $\text{Cu}_{0.5}-(\text{CoO})_{0.5}/\text{TiO}_2$  shown in Fig. 1c further confirms the uniform distribution of Cu, Co, Ti, and O. As marked by the yellow circles, the Cu and Co species are closely connected and form an interface. Moreover, the HRTEM images of  $\text{Cu}/\text{TiO}_2$  and  $\text{CoO}/\text{TiO}_2$  were also recorded. The lattice stripes of Cu can be clearly observed for  $\text{Cu}/\text{TiO}_2$  (Fig. S2c†), but the amorphous CoO of  $\text{CoO}/\text{TiO}_2$  can only be observed vaguely (Fig. S2d†). This characterisation indicates that metallic Cu NPs and CoO with a uniform distribution were successfully synthesised on the  $\text{TiO}_2$  support.

To determine the chemical composition and coordination structure of  $\text{Cu}_{0.5}-(\text{CoO})_{0.5}/\text{TiO}_2$ , XAFS measurements at the Cu and Co K-edges were performed. Fig. 2a shows the Cu K-edge X-ray absorption near-edge structure (XANES) spectra of  $\text{Cu}_{0.5}-(\text{CoO})_{0.5}/\text{TiO}_2$ , Cu foil,  $\text{Cu}_2\text{O}$ , and CuO. It can be seen that the absorption edge of  $\text{Cu}_{0.5}-(\text{CoO})_{0.5}/\text{TiO}_2$  is close to that of the

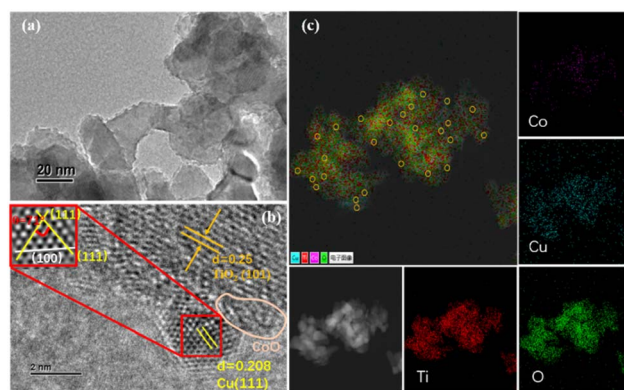


Fig. 1 (a) TEM and (b) HRTEM images and atomic images obtained by local inverse Fourier transform of  $\text{Cu}_{0.5}-(\text{CoO})_{0.5}/\text{TiO}_2$ . (c) EDX elemental mapping images of  $\text{Cu}_{0.5}-(\text{CoO})_{0.5}/\text{TiO}_2$ .





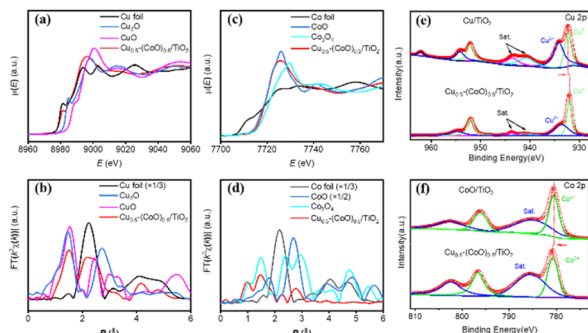


Fig. 2 (a) Normalized XANES spectra and (b) Fourier transformation of EXAFS spectra at the Cu K-edge of  $\text{Cu}_{0.5}-(\text{CoO})_{0.5}/\text{TiO}_2$ , and reference samples of Cu foil,  $\text{Cu}_2\text{O}$  and  $\text{CuO}$ . (c) Normalized XANES spectra and (d) Fourier transformation of EXAFS spectra at the Co-K edge of  $\text{Cu}_{0.5}-(\text{CoO})_{0.5}/\text{TiO}_2$ , and reference samples of Co foil,  $\text{CoO}$  and  $\text{Co}_3\text{O}_4$ . (e) The high-resolution XPS spectra of Cu 2p of  $\text{Cu}/\text{TiO}_2$  and  $\text{Cu}_{0.5}-(\text{CoO})_{0.5}/\text{TiO}_2$ . (f) The high-resolution XPS spectra of Co 2p of  $\text{CoO}/\text{TiO}_2$  and  $\text{Cu}_{0.5}-(\text{CoO})_{0.5}/\text{TiO}_2$ .

Cu foil, indicating that the Cu NPs mainly exist in the metallic state. In addition, the stronger white line of  $\text{Cu}_{0.5}-(\text{CoO})_{0.5}/\text{TiO}_2$  compared with that of the Cu foil suggests that the Cu is partially oxidised on the surface of the particles. Correspondingly, the FT  $k^3$ -weighted extended XAFS (EXAFS)  $\chi(k)$  curve of  $\text{Cu}_{0.5}-(\text{CoO})_{0.5}/\text{TiO}_2$  shows two peaks at 1.50 and 2.20 Å (Fig. 2b). The 1.50 Å peak is located at the same position as the Cu–O peak for  $\text{CuO}$ , and the 2.20 Å peak is at the same position as the metallic Cu–Cu peak of the Cu foil. The apparent presence of metallic Cu–Cu bonds further proves that Cu metal NPs are generated in  $\text{Cu}_{0.5}-(\text{CoO})_{0.5}/\text{TiO}_2$ . The EXAFS FT curve of  $\text{Cu}_{0.5}-(\text{CoO})_{0.5}/\text{TiO}_2$  has a distinctly different spectral shape than that of  $\text{Cu}_2\text{O}$ , especially in the higher-shell R-region beyond 2 Å. Similarly, Fig. 2c–d show the Co K edge XAFS spectra of  $\text{Cu}_{0.5}-(\text{CoO})_{0.5}/\text{TiO}_2$ . The position of the absorption edge of  $\text{Cu}_{0.5}-(\text{CoO})_{0.5}/\text{TiO}_2$  is closer to that of  $\text{CoO}$  than to those of Co foil and  $\text{Co}_3\text{O}_4$ , and the overall spectral shape resembles that of  $\text{CoO}$ , revealing that Co mainly exists in the form of  $\text{CoO}$ . In the EXAFS FT curve in Fig. 2d, two peaks at 1.47 and 2.76 Å can be observed, corresponding to the Co–O and Co–Co bonds in  $\text{CoO}$ , respectively. No metallic Co–Co peak like that for the Co foil at 2.1 Å is visible, indicating the absence of metal Co particles.

To investigate the surface electronic states and interactions of the samples, XPS spectra of  $\text{Cu}_{0.5}-(\text{CoO})_{0.5}/\text{TiO}_2$  and  $\text{Cu}/\text{TiO}_2$  were analysed, with their high-resolution spectra Cu 2p shown in Fig. 2e. For  $\text{Cu}_{0.5}-(\text{CoO})_{0.5}/\text{TiO}_2$ , the peaks at 932.0 and 952.0 eV can be attributed to the  $2p_{3/2}$  and  $2p_{1/2}$  of  $\text{Cu}^0$ , and the peaks at 933.6 and 954.8 eV to the  $2p_{3/2}$  and  $2p_{1/2}$  of  $\text{Cu}^{2+}$ , respectively. The two satellite peaks of  $\text{Cu}^{2+} 2p_{3/2}$  at 940.9 eV and 943.7 eV can also be observed.<sup>26,38</sup> The  $\text{Cu}/\text{TiO}_2$  spectrum features apparent  $\text{Cu}^0$  and  $\text{Cu}^{2+}$  peaks. The peak area ratio of  $\text{Cu}^0:\text{Cu}^{2+}$  increases from 0.6 for  $\text{Cu}/\text{TiO}_2$  to 1.2 for  $\text{Cu}_{0.5}-(\text{CoO})_{0.5}/\text{TiO}_2$ . Compared with  $\text{Cu}/\text{TiO}_2$ , the binding energy of  $\text{Cu}^0 2p_{3/2}$  in  $\text{Cu}_{0.5}-(\text{CoO})_{0.5}/\text{TiO}_2$  shows a slight shift towards a lower energy, from 932.2 to 932.0 eV, suggesting the

presence of electron-rich  $\text{Cu}^0$  in  $\text{Cu}_{0.5}-(\text{CoO})_{0.5}/\text{TiO}_2$ . In addition, high-resolution Co 2p spectra were recorded to determine the oxidation state of CoO in both  $\text{CoO}/\text{TiO}_2$  and  $\text{Cu}_{0.5}-(\text{CoO})_{0.5}/\text{TiO}_2$  (Fig. 2f). The peaks in the spectra at around 780.7 and 796.6 eV, associated with the satellite peaks at 785.5 and 802.5 eV, are characteristic features of the Co  $2p_{3/2}$  and  $2p_{1/2}$  of  $\text{CoO}$ , respectively.<sup>18,39,40</sup> Moreover, the binding energy of Co  $2p_{3/2}$  in  $\text{Cu}_{0.5}-(\text{CoO})_{0.5}/\text{TiO}_2$  (780.7 eV) is 0.2 eV higher than that (780.5 eV) of  $\text{CoO}/\text{TiO}_2$ . The opposite trend in the Cu  $2p_{3/2}$  and Co  $2p_{3/2}$  binding energies is due to the transfer of electrons from CoO to Cu, indicating that the Cu–CoO heterostructure of  $\text{Cu}_{0.5}-(\text{CoO})_{0.5}/\text{TiO}_2$  exhibits strong electronic interactions and interfacial synergism. Similar DFT calculations have been performed in previous studies, which have repeatedly confirmed that electron transfer occurs at the metal oxide interface.<sup>34,41</sup>

### Catalytic performance for $\text{NH}_3\text{BH}_3$ hydrolysis

The catalytic performance of all of the prepared samples in the hydrolytic dehydrogenation of  $\text{NH}_3\text{BH}_3$  was investigated by adding 10 mg of the catalysts to 5 mL of an aqueous solution containing  $\text{NH}_3\text{BH}_3$  (0.325 mmol) at 298 K. If completely hydrolysed, 0.325 mmol of  $\text{NH}_3\text{BH}_3$  yields approximately 21 mL of  $\text{H}_2$  ( $n_{\text{H}_2}/n_{\text{AB}} = 3.0$ ). Fig. 3a shows the time course data of the generation of  $\text{H}_2$  from different samples.  $\text{CoO}/\text{TiO}_2$  exhibits no activity towards the hydrolysis of  $\text{NH}_3\text{BH}_3$ , while  $\text{Cu}/\text{TiO}_2$  shows low activity, indicating that Cu is the effective element for the hydrolysis of  $\text{NH}_3\text{BH}_3$ . In contrast, all the  $\text{Cu}_x-(\text{CoO})_{1-x}/\text{TiO}_2$  ( $x$  ranges from 0.1 to 0.9) samples show much higher catalytic activity, exhibiting a strong synergistic effect between Cu and Co. The hydrolysis performance tests show that the  $\text{Cu}_{0.5}-(\text{CoO})_{0.5}/\text{TiO}_2$  catalyst exhibits the highest catalytic activity, catalysing the hydrolysis reaction in just 174 s. As shown in Fig. 3b, the catalytic activity of the samples was quantified by the TOF values (Table S2†), which show volcano-type activity.  $\text{Cu}/\text{TiO}_2$  has a very low TOF of 1.0  $\text{mol}_{\text{H}_2} \text{mol}_{\text{metal}}^{-1} \text{min}^{-1}$ . When CoO is present, the TOF rises rapidly to 14.9  $\text{mol}_{\text{H}_2} \text{mol}_{\text{metal}}^{-1} \text{min}^{-1}$  for the  $\text{Cu}_{0.9}-(\text{CoO})_{0.1}/\text{TiO}_2$  catalyst with the lowest Co content. A maximum was reached for  $\text{Cu}_{0.5}-(\text{CoO})_{0.5}/\text{TiO}_2$ , the TOF of which of 40.8  $\text{mol}_{\text{H}_2} \text{mol}_{\text{metal}}^{-1} \text{min}^{-1}$  is higher than those of most of the reported Cu-based or other non-noble metal catalysts for  $\text{NH}_3\text{BH}_3$  hydrolysis under the same conditions (Table S3†). With a further increase in Co content, the TOF declines. It is thus

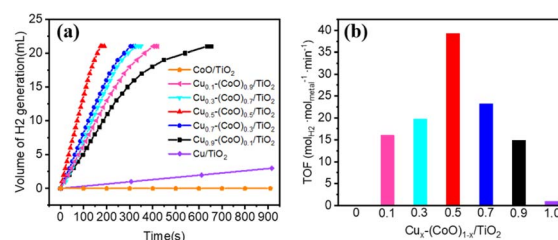


Fig. 3 (a) Hydrogen production over time for the hydrolysis of ammonia borane (0.325 mmol, 5 mL) catalysed by  $\text{Cu}_x-(\text{CoO})_{1-x}/\text{TiO}_2$  samples with different Cu : Co ratios at 298 K. (b) The corresponding TOF value.

reasonable to infer that for  $\text{Cu}_{0.5}\text{-(CoO)}_{0.5}/\text{TiO}_2$  the synergistic effect of the interface between the metal Cu and CoO is the best, leading to this catalyst exhibiting the maximizing efficiency in  $\text{NH}_3\text{BH}_3$  hydrolysis. When the Cu : Co ratio is higher or lower, the interfacial effect of Cu and CoO is weakened, and the catalyst activity is greatly reduced.<sup>34,42</sup>

As  $\text{Cu}_{0.5}\text{-(CoO)}_{0.5}/\text{TiO}_2$  exhibited the highest catalytic activity for the hydrolysis of  $\text{NH}_3\text{BH}_3$ , it was selected for further kinetic studies at different reaction temperatures, catalyst concentrations, and  $\text{NH}_3\text{BH}_3$  concentrations. Fig. 4a shows the effect that temperature has on  $\text{NH}_3\text{BH}_3$  hydrolysis. As the temperature increases from 298 to 313 K, the  $\text{H}_2$  evolution activity increases. According to the Arrhenius plot shows in Fig. 4b and the Arrhenius equation, the  $E_a$  value of  $\text{Cu}_{0.5}\text{-(CoO)}_{0.5}/\text{TiO}_2$  for the hydrolysis of  $\text{NH}_3\text{BH}_3$  is  $48.1 \text{ kJ mol}^{-1}$ . Fig. S3† shows the influence of catalyst concentration on the reaction rate, which was measured by varying the amount of  $\text{Cu}_{0.5}\text{-(CoO)}_{0.5}/\text{TiO}_2$  from 10 to 25 mg. As the amount of catalyst increases, the rate of  $\text{H}_2$  production increases. The slope of  $\ln(\text{rate})$  versus  $\ln(\text{catalyst amount})$  curve is 1.0, indicating that the catalytic hydrolysis of  $\text{NH}_3\text{BH}_3$  is a first-order reaction relative to the catalyst concentration. The effect that  $\text{NH}_3\text{BH}_3$  concentration has on the  $\text{H}_2$  production rate was measured (Fig. S4†), and the volume of  $\text{H}_2$  was found to increase in line with an increase in the  $\text{NH}_3\text{BH}_3$  content, but the initial rate of  $\text{H}_2$  production remained the same. The relationship between the  $\text{H}_2$  production rate and the corresponding  $\text{NH}_3\text{BH}_3$  concentration was determined on the natural logarithmic scale, and the slope of the curve was measured as 0.073, suggesting that the hydrolysis of  $\text{NH}_3\text{BH}_3$  catalysed by  $\text{Cu}_{0.5}\text{-(CoO)}_{0.5}/\text{TiO}_2$  is a zero-order reaction with respect to the concentration of  $\text{NH}_3\text{BH}_3$ . In summary, the hydrolysis of  $\text{NH}_3\text{BH}_3$  is facilitated by  $\text{Cu}_{0.5}\text{-(CoO)}_{0.5}/\text{TiO}_2$  catalyst and is independent of the  $\text{NH}_3\text{BH}_3$  concentration.

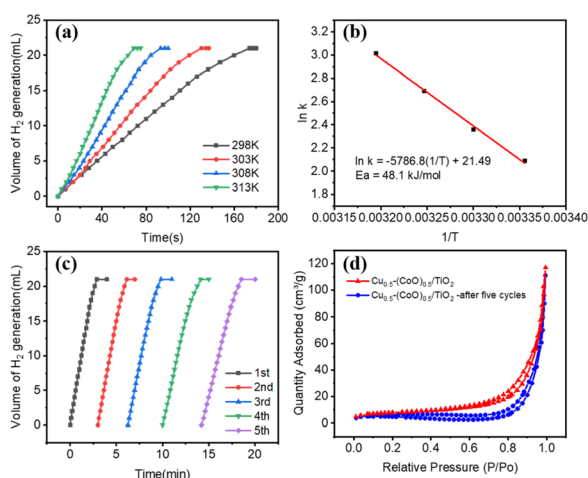


Fig. 4 (a)  $\text{H}_2$  production over time for the hydrolysis of  $\text{NH}_3\text{BH}_3$  catalysed by  $\text{Cu}_{0.5}\text{-(CoO)}_{0.5}/\text{TiO}_2$  at different temperatures. (b) The corresponding Arrhenius plot and the  $E_a$ . (c) Recyclability testing of  $\text{Cu}_{0.5}\text{-(CoO)}_{0.5}/\text{TiO}_2$  as a catalyst in the hydrolysis of  $\text{NH}_3\text{BH}_3$  for five cycles. (d)  $\text{N}_2$  adsorption-desorption isotherms of  $\text{Cu}_{0.5}\text{-(CoO)}_{0.5}/\text{TiO}_2$  before and after five cycles.

The stability of a catalyst is the key to its practical application. With this in mind, the recyclability of  $\text{Cu}_{0.5}\text{-(CoO)}_{0.5}/\text{TiO}_2$  was tested by adding an additional aqueous solution of  $\text{NH}_3\text{BH}_3$  (0.325 mmol, 5 mL) at room temperature after the previous reaction was completed, with the results shown in Fig. 4c. It can be seen that the total  $\text{H}_2$  production does not change, but the rate of  $\text{H}_2$  generation gradually slows down. This shows that the catalyst has relatively high stability and can catalyse the complete hydrolysis of  $\text{NH}_3\text{BH}_3$ , but that the activity decreases slightly. After five cycles, the activity of  $\text{Cu}_{0.5}\text{-(CoO)}_{0.5}/\text{TiO}_2$  is still 67% that of the original value. To explore the causes behind the decrease in the catalyst activity, nitrogen ( $\text{N}_2$ ) adsorption-desorption isotherm experiments were conducted to determine the specific surface area of the  $\text{Cu}_{0.5}\text{-(CoO)}_{0.5}/\text{TiO}_2$  catalyst before and after five catalytic cycles. Fig. 4d shows the BET curves plotted over a relative pressure range of 0–1.0 ( $P/P_0$ ). The BET specific surface area of  $\text{Cu}_{0.5}\text{-(CoO)}_{0.5}/\text{TiO}_2$  is  $27.22 \text{ m}^2 \text{ g}^{-1}$ , which decreased to  $12.54 \text{ m}^2 \text{ g}^{-1}$  after five cycles of hydrolysis reactions. The decrease in the specific surface area of  $\text{Cu}_{0.5}\text{-(CoO)}_{0.5}/\text{TiO}_2$  indicated that the support and metal NPs agglomerated, leading to a reduction in the number of active sites of the catalyst, which may have led to the decrease in its catalytic activity. In addition, the PXRD and TEM data of  $\text{Cu}_{0.5}\text{-(CoO)}_{0.5}/\text{TiO}_2$  were recorded after five cycles. As shown in Fig. S5a,† no diffraction peaks of Cu and Co can be observed in the PXRD pattern  $\text{Cu}_{0.5}\text{-(CoO)}_{0.5}/\text{TiO}_2$ , indicating that the particles of  $\text{Cu}_{0.5}\text{-(CoO)}_{0.5}/\text{TiO}_2$  after the reaction are small or amorphous. The TEM image shown in Fig. S5b† indicates that some  $\text{Cu}_{0.5}\text{-(CoO)}_{0.5}/\text{TiO}_2$  aggregates into larger particles, which may be another reason its reduced catalytic efficiency after reaction. In addition, there may be some other possible reasons behind the reduced catalytic efficiency of  $\text{Cu}_{0.5}\text{-(CoO)}_{0.5}/\text{TiO}_2$ . Firstly, an increase in the number of cycles, the concentration of the reactants is diluted, and the by-products generated accumulate, hindering the forward reaction. Secondly, the increase in the by-products gradually leads to an increase in solution viscosity, which slows the reaction. Moreover, a large number of boronised species produced in the reaction cover the surface of the catalyst, reducing the catalytic efficiency.

### Study on hydrolytic mechanism of $\text{NH}_3\text{BH}_3$

It has been proposed in several studies that the cleavage of the O–H bond in the  $\text{H}_2\text{O}$  molecule is the rate-determining step in the hydrolysis of  $\text{NH}_3\text{BH}_3$ .<sup>43–47</sup> To further elucidate this mechanism and facilitate the rational design of the catalyst, isotopic experiments on the  $\text{Cu}_{0.5}\text{-(CoO)}_{0.5}/\text{TiO}_2$  catalyst were conducted using  $\text{D}_2\text{O}$  instead of  $\text{H}_2\text{O}$ . The kinetic isotope effect (KIE) was used to reveal whether water is the rate-determining step in this reaction, with the results shown in Fig. 5a. The hydrolysis of  $\text{NH}_3\text{BH}_3$  in  $\text{D}_2\text{O}$  exhibits a slower rate of  $\text{H}_2$  release and a longer reaction time compared to that of  $\text{NH}_3\text{BH}_3$  in  $\text{H}_2\text{O}$ . The KIE value ( $\text{H}_2\text{O}$  rate/ $\text{D}_2\text{O}$  rate) was calculated to be 5.5.

To further explore the effect of  $\text{OH}^-$  on  $\text{NH}_3\text{BH}_3$  hydrolysis, a series of experiments were conducted at different concentrations of NaOH to test the catalytic performance of  $\text{Cu}_{0.5}\text{-(CoO)}_{0.5}/\text{TiO}_2$ . As shown in Fig. 5b, with an increase in

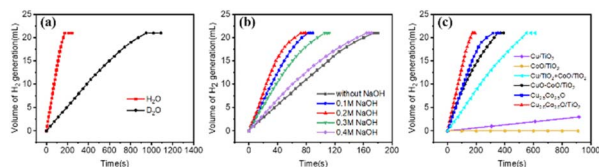


Fig. 5 Hydrolysis of ammonia borane catalysed by  $\text{Cu}_{0.5}-(\text{CoO})_{0.5}/\text{TiO}_2$  (a) in different solutions ( $\text{H}_2\text{O}$  or  $\text{D}_2\text{O}$ ), and (b) in different concentrations of NaOH from 0.1 to 0.4 M, at 298 K. (c) Hydrogen production over time for the hydrolysis of ammonia borane (0.325 mmol, 5 mL) catalysed by different samples.

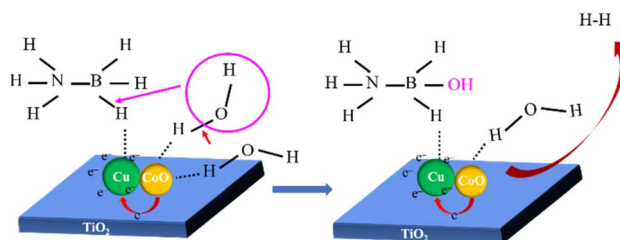
NaOH concentration, the  $\text{H}_2$  release rate gradually accelerates. When the concentration of NaOH is 0.2 M, the TOF reaches a maximum value of  $104.0 \text{ mol}_{\text{H}_2} \text{ mol}_{\text{metal}}^{-1} \text{ min}^{-1}$ , which exceeds the TOF values of most non-noble metal catalysts for the same reaction (Table S3<sup>†</sup>). In 0.2 M NaOH, the apparent activation energy,  $E_a$ , is estimated to be  $24.28 \text{ kJ mol}^{-1}$  (Fig. S6<sup>†</sup>), significantly lower than the  $E_a$  of  $48.1 \text{ kJ mol}^{-1}$  recorded in the absence of NaOH. These results indicate that  $\text{OH}^-$  provided by NaOH promotes the catalytic reaction. On the one hand,  $\text{OH}^-$  adsorption on the catalyst surface increases electron density, which is conducive to the attack on the reactants and accelerates the intermediate reaction. On the other hand,  $\text{OH}^-$  provides more adsorbed O–H, accelerating the oxidation addition reaction of water.<sup>17,48,49</sup> However, when the concentration of NaOH exceeds 0.2 M, the catalytic rate decreases. This may be due to the excess  $\text{OH}^-$  species overlaying the active sites originally used for H coordination and  $\text{H}_2$  dissociation.<sup>15,31</sup> The rate of generation of  $\text{H}_2$  was found to be generally accelerated by NaOH, supporting that the rate-determining step in the hydrolysis reaction is the cleavage of the O–H bond in  $\text{H}_2\text{O}$ .

Based on the above results, it is reasonable to conclude that the excellent performance of  $\text{Cu}_{0.5}-(\text{CoO})_{0.5}/\text{TiO}_2$  in the hydrolysis of  $\text{NH}_3\text{BH}_3$  can be attributed to the strong interfacial interaction of Cu–CoO, which accelerates the rate-determining step. To further verify this conclusion, comparison experiments were conducted, and the results are shown in Fig. 5c. Such interfacial effects may also be observed upon physically mixing the two components; thus, it is of interest to observe how the catalysts behave when mixed. For this purpose,  $\text{Cu}/\text{TiO}_2$  and  $\text{CoO}/\text{TiO}_2$  were mechanically mixed and tested under the same conditions. As observed from Table S2,<sup>†</sup> the mixed  $\text{Cu}/\text{TiO}_2 + \text{CoO}/\text{TiO}_2$  catalyst has a TOF value of  $9.9 \text{ mol}_{\text{H}_2} \text{ mol}_{\text{metal}}^{-1} \text{ min}^{-1}$ , higher than those of  $\text{Cu}/\text{TiO}_2$  or  $\text{CoO}/\text{TiO}_2$  alone, but far less than that of  $\text{Cu}_{0.5}-(\text{CoO})_{0.5}/\text{TiO}_2$ . As expected, the interfacial contact between Cu and CoO in the mechanically mixed NPs gives rise to an interfacial synergy that increases the reaction rate. However, the interfacial contact between  $\text{Cu}/\text{TiO}_2$  and  $\text{CoO}/\text{TiO}_2$  is limited, meaning that its activity is far worse than that of  $\text{Cu}_{0.5}-(\text{CoO})_{0.5}/\text{TiO}_2$  comprised of closely connected Cu–CoO. In terms of Cu–CoO, the presence of electron-rich Cu is conducive to the attack and activation of  $\text{NH}_3\text{BH}_3$ ,<sup>19,31,50,51</sup> and CoO enhances the adsorption of  $\text{H}_2\text{O}$ , thus speeding up the rate-determining step of the reaction, leading to an improvement in

the activity of the catalyst in a bifunctional way to achieve the best reaction efficiency.

As previously mentioned, some of the Cu atoms in the  $\text{Cu}_{0.5}-(\text{CoO})_{0.5}/\text{TiO}_2$  catalyst are oxidised. Given that interfacial sites play essential roles in  $\text{NH}_3\text{BH}_3$  hydrolysis, the enhanced  $\text{H}_2$  generation rate may be attributed to CuO–CoO interfacial sites. To clarify this point, a control experiment was conducted by synthesising a  $\text{CuO-CoO}/\text{TiO}_2$  sample with similar Cu and Co content to  $\text{Cu}_{0.5}-(\text{CoO})_{0.5}/\text{TiO}_2$ , and it was characterised by PXRD (Fig. S7<sup>†</sup>) and XPS (Fig. S8<sup>†</sup>). The Cu 2p and Co 2p spectra, as well as the content of each element measured by XPS (Table S4<sup>†</sup>), indicate the presence of CuO and CoO in  $\text{CuO-CoO}/\text{TiO}_2$ . The catalytic performance of  $\text{CuO-CoO}/\text{TiO}_2$  was then investigated (Table S2<sup>†</sup>). The attained TOF value of  $19.0 \text{ mol}_{\text{H}_2} \text{ mol}_{\text{metal}}^{-1} \text{ min}^{-1}$  is much better than those of  $\text{Cu}/\text{TiO}_2$  and  $\text{CoO}/\text{TiO}_2$ , as the CuO/CoO interface activates  $\text{H}_2\text{O}$  and accelerates the rate-determining step of the reaction.<sup>34,52,53</sup> However, the TOF of  $\text{CuO-CoO}/\text{TiO}_2$  is still significantly inferior to that of  $\text{Cu}_{0.5}-(\text{CoO})_{0.5}/\text{TiO}_2$ , indicating that the heterogeneous structure of Cu–CoO compared with that of CuO–CoO plays a major and decisive role in promoting the reaction. In addition, to explore the role of the  $\text{TiO}_2$  support, a support-free  $\text{Cu}_{0.5}-(\text{CoO})_{0.5}$  catalyst was prepared, and performance testing was conducted under the same conditions. The  $\text{H}_2$  production rate of  $\text{Cu}_{0.5}-(\text{CoO})_{0.5}$  was observed to be poor (Fig. 5c) and its TOF value was only  $2.4 \text{ mol}_{\text{H}_2} \text{ mol}_{\text{metal}}^{-1} \text{ min}^{-1}$  (Table S2<sup>†</sup>), much lower than that of  $\text{Cu}_{0.5}-(\text{CoO})_{0.5}/\text{TiO}_2$ . This shows that the addition of the  $\text{TiO}_2$  support improves the dispersion of Cu and CoO NPs by inhibiting NP aggregation and exposing more active sites, which is conducive to promoting the catalytic reaction.

A possible catalytic synergistic mechanism of  $\text{NH}_3\text{BH}_3$  hydrolysis catalysed by  $\text{Cu}_{0.5}-(\text{CoO})_{0.5}/\text{TiO}_2$  catalyst was proposed (Scheme 1). Firstly, the strong interfacial interaction results in unbalanced electron distribution on the surface of Cu–CoO, which accelerates and activates the adsorption of  $\text{NH}_3\text{BH}_3$  and  $\text{H}_2\text{O}$  on the surface of Cu and CoO, respectively, thus reducing the reaction energy barrier.<sup>41,54</sup> Secondly, the O–H bond of the activated  $\text{H}_2\text{O}$  molecule breaks, with the formation of  $\text{H}^*$  and  $\text{OH}^*$ . Then,  $\text{OH}^*$  attacks and breaks the B–H bond of  $\text{NH}_3\text{BH}_3$  to form  $\text{NH}_3\text{BH}_2\text{-OH}$  accompanied by the release of  $\text{H}^*$ , which combines with another  $\text{H}^*$  released by  $\text{H}_2\text{O}$  to generate 1 mol of  $\text{H}_2$  at the surface of the  $\text{Cu}_{0.5}-(\text{CoO})_{0.5}/\text{TiO}_2$  catalyst. At the same time, the second  $\text{H}_2\text{O}$  molecule adsorbed



Scheme 1 A proposed mechanism for ammonia borane hydrolysis over the  $\text{Cu}_{0.5}-(\text{CoO})_{0.5}/\text{TiO}_2$  catalyst.





on CoO is activated, and the above steps are repeated until 3 mol of H<sub>2</sub> is finally released from the catalyst surface. In the catalytic process, the strong interaction between Cu and CoO makes promotes the adsorption and activation of NH<sub>3</sub>BH<sub>3</sub> and H<sub>2</sub>O, reducing the energy barrier of the entire reaction and accelerating the release rate of H<sub>2</sub> in the catalytic reaction. Therefore, the unique metal and metal oxide structures in the Cu<sub>0.5</sub>–(CoO)<sub>0.5</sub>/TiO<sub>2</sub> catalyst play an important synergistic role in accelerating reactant activation. The support TiO<sub>2</sub> ensures the dispersion and stability of the active sites during the reaction. The overall coordination of the catalyst greatly improves the catalytic performance of H<sub>2</sub> production from NH<sub>3</sub>BH<sub>3</sub>.

## Conclusions

In summary, metallic Cu NPs and oxidised CoO NPs were successfully loaded on a TiO<sub>2</sub> support *via* simple incipient wetness impregnation and co-reduction methods. The optimum Cu<sub>0.5</sub>–(CoO)<sub>0.5</sub>/TiO<sub>2</sub> catalyst exhibits high activity and stability in the hydrolysis of NH<sub>3</sub>BH<sub>3</sub>, with a TOF value of 104.0 mol<sub>H<sub>2</sub></sub> mol<sub>metal</sub><sup>–1</sup> min<sup>–1</sup> in 0.2 M NaOH at room temperature, which is better than the performance of most reported non-noble metal catalysts. The synergistic interface of Cu–CoO accelerates the oxidative cleavage of the O–H bonds in H<sub>2</sub>O (the rate-determining step) and the activation of NH<sub>3</sub>BH<sub>3</sub> molecules, thus increasing the hydrolysis rate of NH<sub>3</sub>BH<sub>3</sub>. This study demonstrates the high efficiency of the interface structure of metal and transition metal oxides for hydrolytic dehydrogenation of ammonia borane, which can also be applied to many other homogeneous or heterogeneous catalytic hydrogen production reactions, such as NaBH<sub>4</sub> hydrolysis and electrocatalytic hydrogen evolution reactions, providing a simple and reliable strategy for the development of non-precious metal catalysts.

## Author contributions

Hongmei Li: conceptualization, methodology, writing – original draft. Wenxue He: investigation, resources. Liuxin Xu: data curation. Ya Pan: validation, visualization. Ruichao Xu: formal analysis, data curation. Zhihu Sun: writing – review & editing, funding acquisition. Shiqiang Wei: supervision, project administration.

## Conflicts of interest

The authors declare that they have no competing financial interests.

## Acknowledgements

The authors thank National Key Research and Development Program of China (No. 2021YFA1500403), the National Natural Science Foundation of China (Grant No. 12075243 and 12135012) for financial support. They also greatly appreciate the synchrotron radiation beam times of SSRF and BSRF.

## Notes and references

- 1 I. P. Jain, *Int. J. Hydrogen Energy*, 2009, **34**, 7368–7378.
- 2 S. Sharma and S. K. Ghoshal, *Renewable Sustainable Energy Rev.*, 2015, **43**, 1151–1158.
- 3 S. E. Hosseini and M. A. Wahid, *Renewable Sustainable Energy Rev.*, 2016, **57**, 850–866.
- 4 E. Antolini, *RSC Adv.*, 2016, **6**, 3307–3325.
- 5 A. M. Abdalla, S. Hossain, O. B. Nisfindy, A. T. Azad, M. Dawood and A. K. Azad, *Energy Convers. Manage.*, 2018, **165**, 602–627.
- 6 C. Wang and D. Astruc, *Chem. Soc. Rev.*, 2021, **50**, 3437–3484.
- 7 Y. Ma, X. R. Wang, T. Li, J. Zhang, J. Gao and Z. Y. Sun, *Int. J. Hydrogen Energy*, 2021, **46**, 27330–27348.
- 8 C. Lang, Y. Jia and X. Yao, *Energy Storage Mater.*, 2020, **26**, 290–312.
- 9 Z. Lin, B. Xiao, Z. Wang, W. Tao, S. Shen, L. Huang, J. Zhang, F. Meng, Q. Zhang, L. Gu and W. Zhong, *Adv. Funct. Mater.*, 2021, **31**, 2102321.
- 10 A. Rossin and M. Peruzzini, *Chem. Rev.*, 2016, **116**, 8848–8872.
- 11 C. Y. Peng, L. Kang, S. Cao, Y. Chen, Z. S. Lin and W. F. Fu, *Angew. Chem., Int. Ed.*, 2015, **54**, 15725–15729.
- 12 J. Manna, S. Akbayrak and S. Özkaz, *Appl. Catal., B*, 2017, **208**, 104–115.
- 13 X. Huang, Y. Liu, H. Wen, R. Shen, S. Mehdi, X. Wu, E. Liang, X. Guo and B. Li, *Appl. Catal., B*, 2021, **287**, 119960.
- 14 S. Rej, L. Mascaretti, E. Y. Santiago, O. Tomanec, Š. Kment, Z. Wang, R. Zbořil, P. Fornasiero, A. O. Govorov and A. Naldoni, *ACS Catal.*, 2020, **10**, 5261–5271.
- 15 F. Fu, C. Wang, Q. Wang, A. M. Martinez-Villacorta, A. Escobar, H. Chong, X. Wang, S. Moya, L. Salmon, E. Fouquet, J. Ruiz and D. Astruc, *J. Am. Chem. Soc.*, 2018, **140**, 10034–10042.
- 16 J. Zhang, Y. Wang, Y. Zhu, G. Mi, X. Du and Y. Dong, *Renewable Energy*, 2018, **118**, 146–151.
- 17 C. Wang, J. Tuninetti, Z. Wang, C. Zhang, R. Ciganda, L. Salmon, S. Moya, J. Ruiz and D. Astruc, *J. Am. Chem. Soc.*, 2017, **139**, 11610–11615.
- 18 S. Mehdi, Y. Liu, H. Wei, H. Wen, R. Shen, Z. Peng, H. Zhang, X. Wu, C. Wang, S. Guan, T. Liu and B. Li, *ACS Appl. Nano Mater.*, 2022, **5**, 5064–5074.
- 19 J. Wang, Y. Chen, S. Guan, J. Shi, M. Li and B. Liu, *J. Alloys Compd.*, 2022, **913**, 165215.
- 20 Y. Feng, X. Zhang, Y. Shao, X. Chen, H. Wang, J. Li, M. Wu, H. Dong, Q. Liu and H. Li, *ACS Appl. Mater. Interfaces*, 2022, **14**, 27979–27993.
- 21 J. Liao, Y. Shao, Y. Feng, J. Zhang, C. Song, W. Zeng, J. Tang, H. Dong, Q. Liu and H. Li, *Appl. Catal., B*, 2023, **320**, 121973.
- 22 J. Liao, Y. Wu, Y. Shao, Y. Feng, X. Zhang, W. Zhang, J. Li, M. Wu, H. Dong, Q. Liu and H. Li, *Chem. Eng. J.*, 2022, **449**, 137755.
- 23 Y. Feng, Y. Li, Q. Liao, W. Zhang, Z. Huang, X. Chen, Y. Shao, H. Dong, Q. Liu and H. Li, *Fuel*, 2023, **332**, 126045.



- 24 P. Li, X. Zhang, J. Wang, B. Xu, X. Zhang, G. Fan, L. Zhou, X. Liu, K. Zhang and W. Jiang, *Colloids Surf.*, 2021, **629**, 127383.
- 25 K. Guo, Y. Ding, J. Luo, M. Gu and Z. Yu, *ACS Appl. Energy Mater.*, 2019, **2**, 5851–5861.
- 26 P. Zhang, G. Zeng, T. Song, S. Huang, T. Wang and H. Zeng, *Appl. Catal., B*, 2019, **242**, 389–396.
- 27 J. Li, Q.-L. Zhu and Q. Xu, *Catal. Sci. Technol.*, 2015, **5**, 525–530.
- 28 J.-M. Yan, Z.-L. Wang, H.-L. Wang and Q. Jiang, *J. Mater. Chem.*, 2012, **22**, 10990.
- 29 Y. Liu, J. Zhang, H. Guan, Y. Zhao, J.-H. Yang and B. Zhang, *Appl. Surf. Sci.*, 2018, **427**, 106–113.
- 30 X. Yang, Q. Li, L. Li, J. Lin, X. Yang, C. Yu, Z. Liu, Y. Fang, Y. Huang and C. Tang, *J. Power Sources*, 2019, **431**, 135–143.
- 31 C. Wang, Y. Ren, J. Zhao, S. Sun, X. Du, M. Wang, G. Ma, H. Yu, L. Li, X. Yu, X. Zhang, Z. Lu and X. Yang, *Appl. Catal., B*, 2022, **314**, 121494.
- 32 A. Singh and L. Spiccia, *Coord. Chem. Rev.*, 2013, **257**, 2607–2622.
- 33 J. Zhou, X. Feng, Y. Zhao, R. Cui, D. Wang and B. Zhang, *J. Alloys Compd.*, 2022, **923**, 166345.
- 34 W. Xu, S. Zhang, R. Shen, Z. Peng, B. Liu, J. Li, Z. Zhang and B. Li, *Energy Environ. Mater.*, 2022, 1–7.
- 35 W. He, X. Zhang, K. Zheng, C. Wu, Y. Pan, H. Li, L. Xu, R. Xu, W. Chen, Y. Liu, C. Wang, Z. Sun and S. Wei, *Angew. Chem., Int. Ed.*, 2022, e202213365.
- 36 G. Yang, S. Guan, S. Mehdi, Y. Fan, B. Liu and B. Li, *Green Energy Environ.*, 2021, **6**, 236–243.
- 37 M. Newville, *J. Synchrotron Radiat.*, 2001, **8**, 322–324.
- 38 J. Liao, D. Lu, G. Diao, X. Zhang, M. Zhao and H. Li, *ACS Sustainable Chem. Eng.*, 2018, **6**, 5843–5851.
- 39 Y. Pan, L. Xu, L. Huang, W. He, H. Li, S. Wang, Z. Long and Z. Sun, *ACS Appl. Energy Mater.*, 2021, **4**, 11151–11161.
- 40 Y. Pan, L. Xu, W. He, H. Li, W. Chen and Z. Sun, *Nanoscale*, 2022, **14**, 7303–7313.
- 41 S. Guan, Y. Guo, H. Zhang, X. Liu, Y. Fan and B. Liu, *Sustainable Energy Fuels*, 2022, **6**, 1753–1761.
- 42 J. Manna, S. Akbayrak and S. Özkar, *RSC Adv.*, 2016, **6**, 102035–102042.
- 43 Y. Ge, X. Qin, A. Li, Y. Deng, L. Lin, M. Zhang, Q. Yu, S. Li, M. Peng, Y. Xu, X. Zhao, M. Xu, W. Zhou, S. Yao and D. Ma, *J. Am. Chem. Soc.*, 2021, **143**, 628–633.
- 44 F. Tong, X. Liang, M. Liu, Z. Wang, Y. Liu, P. Wang, H. Cheng, Y. Dai, Z. Zheng and B. Huang, *ACS Catal.*, 2022, **12**, 3558–3565.
- 45 M. H. Fang, S. Y. Wu, Y. H. Chang, M. Narwane, B. H. Chen, W. L. Liu, D. Kurniawan, W. H. Chiang, C. H. Lin, Y. C. Chuang, I. J. Hsu, H. T. Chen and T. T. Lu, *ACS Appl. Mater. Interfaces*, 2021, **13**, 47465–47477.
- 46 Z. Li, T. He, L. Liu, W. Chen, M. Zhang, G. Wu and P. Chen, *Chem. Sci.*, 2017, **8**, 781–788.
- 47 S. Chen, B. Gong, J. Gu, Y. Lin, B. Yang, Q. Gu, R. Jin, Q. Liu, W. Ying, X. Shi, W. Xu, L. Cai, Y. Li, Z. Sun, S. Wei, W. Zhang and J. Lu, *Angew. Chem., Int. Ed.*, 2022, **61**, e202211919.
- 48 J. Deng, X. Zhou, J. Zou, Y. Qin and P. Wang, *ACS Appl. Energy Mater.*, 2022, **5**, 7408–7419.
- 49 Q. Yao, K. Yang, X. Hong, X. Chen and Z.-H. Lu, *Catal. Sci. Technol.*, 2018, **8**, 870–877.
- 50 P. Li, R. Chen, S. Zhao, W. Li, Y. Lin and Y. Yu, *Appl. Catal., B*, 2021, **298**, 120523.
- 51 S. Zhang, M. Li, L. Li, F. Dushimimana, J. Zhao, S. Wang, J. Han, X. Zhu, X. Liu, Q. Ge and H. Wang, *ACS Catal.*, 2020, **10**, 14903–14915.
- 52 K. Feng, J. Zhong, B. Zhao, H. Zhang, L. Xu, X. Sun and S. T. Lee, *Angew. Chem., Int. Ed. Engl.*, 2016, **55**, 11950–11954.
- 53 H. Zheng, K. Feng, Y. Shang, Z. Kang, X. Sun and J. Zhong, *Inorg. Chem. Front.*, 2018, **5**, 1180–1187.
- 54 J. Li, X. Ren, H. Lv, Y. Wang, Y. Li and B. Liu, *J. Hazard. Mater.*, 2020, **391**, 122199.

